Empirical modeling of plasma sheet pressure and three-dimensional force-balanced magnetospheric magnetic field structure: 2. Modeling

Chao Yue,[1] Chih-Ping Wang,[1] Sorin G. Zaharia,[2] Xiaoyan Xing,[1] and Larry Lyons [1]

Received 12 April 2013; revised 27 September 2013; accepted 7 October 2013; published 31 October 2013.

[1] The magnetic field configuration is crucial to plasma sheet dynamics and magnetosphere-ionosphere coupling. In this study we established 3-D force-balanced magnetic fields and investigated configuration changes with *Kp* and solar wind dynamic pressure (P_{SW}). Pressure distributions from the empirical model developed in Wang et al. (2013) were used for obtaining the force-balanced field. Based on our model results, we found that (1) higher P_{SW} mainly enhances pressure in the tail plasma sheet, while larger convection during higher *Kp* drives plasma sheet further earthward, resulting in a pressure increase closer to the Earth; (2) comparing with the magnetic field changes due to increasing P_{SW}, the *Kp* associated pressure enhancement causes the azimuthal current density (J_φ) peak and field-aligned currents (FACs) to move deeper earthward, the magnetic field to decrease further near Earth but increase more in the tail, and field lines to stretch more significantly; (3) as *Kp* and P_{SW} change, the whole plasma sheet remains stable to interchange instability but may be ballooning unstable in the midnight region at *X* between −15 and −10 R_E; (4) the force-balanced configurations are characteristically different from the non-force-balanced Tsyganenko 89 (T89) magnetic field. A region of positive d*Bz*/d*z* in the near-Earth region, which has been observed, is seen in our field but not in T89. On the other hand, a local equatorial *Bz* minimum is predicted by T89 but not by our model. J_ϕ bifurcation appears in the near-Earth region as a result of our J_ϕ configuration being approximately aligned with field lines, while the T89 J_ϕ everywhere decreases monotonically with increasing Z by construction.

Citation: Yue, C., C.-P. Wang, S. G. Zaharia, X. Xing, and L. Lyons (2013), Empirical modeling of plasma sheet pressure and three-dimensional force-balanced magnetospheric magnetic field structure: 2. Modeling, *J. Geophys. Res. Space Physics*, *118*, 6166–6175, doi:10.1002/2013JA018943.

1. Introduction

[2] In the Earth's plasma sheet, plasma pressure is comparable to (and many times larger than) the magnetic field pressure. As a result, the magnetic field has a stretched configuration that generates a magnetic curvature force to balance the total pressure gradient force. This coupling between magnetic field and plasma plays a crucial role in the particle dynamics and energization in magnetosphere-ionosphere (M-I) coupling, and thus also in the plasma sheet processes causing geomagnetic disturbances. Better understanding of these processes relies on knowing more accurately the magnetic field configuration. The goal of this study is to establish a realistic 3-D magnetic field configuration that satisfies the physical constraint of force balance with observed plasma pressure distributions obtained in the companion paper [*Wang et al.*, 2013].

[3] Past studies on large-scale plasma sheet pressure and magnetic field distributions [e.g., *Spence et al.*, 1989; *Kistler et al.*, 1993; *Hori et al.*, 2000; *Kaufmann et al.*, 2001] have shown that the structures and the associated plasma sheet dynamics change significantly under different solar wind and geomagnetic conditions. The pressure and magnetic field are closely coupled through force balance. The magnetic field configuration affects particles in their motion [e.g., *Speiser*, 1965] and pitch-angle distributions [e.g., *Sergeev et al.*, 1983], as well as their energization [e.g., *Wang et al.*, 2004]. In return the resulting plasma pressure changes the magnetic field. The coupling may lead to possible instabilities [*Xing and Wolf*, 2007; *Cheng and Lui*, 1998] that locally and temporarily disrupt the plasma and magnetic field equilibrium. These processes in the plasma sheet can connect with ionospheric processes through magnetic field-aligned currents (FACs). Therefore, magnetic field models have been widely used for evaluating various plasma sheet dynamics and instabilities with observations

This article is a companion to *Wang* [2013], doi:10.1002/jgra.50585.

[1]Department of Atmospheric and Oceanic Sciences, University of California, Los Angeles, California, USA.
[2]Space Science and Applications, Los Alamos National Laboratory, Los Alamos, New Mexico, USA.

Corresponding author: C. Yue, Department of Atmospheric and Oceanic Sciences, UCLA, Los Angeles, CA, USA. (yuechao@atmos.ucla.edu)

2169-9380/13/10.1002/2013JA018943

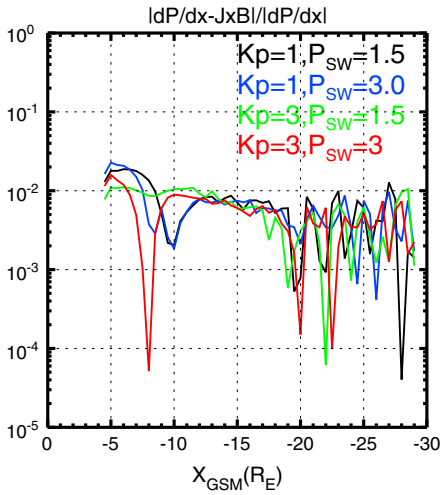

Figure 1. Illustration of achievement of force balance (plotted is the normalized residual force imbalance at midnight on the equatorial plane).

and simulations, as well as for mapping plasma sheet features to observed ionospheric phenomena [e.g., *Sergeev and Malkov*, 1988; *Wing and Newell*, 1998].

[4] Most of the empirical magnetic field models [e.g., *Olson and Pfitzer*, 1974; *Tsyganenko*, 1995, 1996] were established by fitting the model magnetic field generated from a framework of postulated electrical currents to numerous observations at different locations and times. While empirical models provide realistic large-scale fields, they do not have built-in force balance between field and plasma pressure, as force balance imposes additional constraints [*Zaharia and Cheng*, 2003]. The empirical models have also been shown [e.g., *McCollough et al.*, 2008] to perform well only in certain areas or under certain geomagnetic conditions. These drawbacks certainly lead to larger uncertainties in the results using these models. For example, errors in mapping latitudes can wrongly link an ionospheric phenomenon with an unrelated process or region in the magnetotail.

[5] As a step toward solving this problem, a first principle calculation of magnetospheric equilibrium can be utilized to study the magnetic field configurations under specific solar wind or geomagnetic conditions. This approach is very important in regions of large plasma beta (ratio of plasma to magnetic pressure), such as the plasma sheet, where magnetic field and plasma pressure are strongly coupled. Force balance is valid in the slow flow region of the magnetosphere, in which quasi-static equilibrium is believed to exist most of the time [*Wolf*, 1983] except for short periods of explosive activity [e.g., *Tsyganenko*, 1990]. In equilibrium, both magnetic field and plasma pressure evolve while maintaining (approximate) force balance with each other. *Tsyganenko* [2010] reconstructed the magnetospheric plasma pressure distributions in the midnight meridian plane from four empirical Tsyganenko magnetic field models through approximate (in a least square sense) force balance equation. They found that the T89 and T96 models give more realistic inferred pressure than do TU82 and T87, the inferred pressure being nearly isotropic in the tail, with a moderate pancake-type anisotropy in the inner magnetosphere, consistent with observations.

[6] Present force balance magnetic field modeling includes methods using the MHD approach of numerical relaxation technique [*Hesse and Birn*, 1993; *Toffoletto et al.*, 2001], the Biot-Savart approach with magnetic field obtained from flexible current density distributions [*Wang et al.*, 2002], and various Euler-potential approaches [*Cheng*, 1995; *Zaharia et al.*, 2004; *Liu et al.*, 2006; *Gkioulidou et al.*, 2011]. In the Euler-potential approach, the magnetic field $\mathbf{B}=\nabla\alpha\times\nabla\beta$ is determined by two Euler potentials α and β. *Zaharia* [2008] developed a new Euler-potential method for solving a three-dimensional (3-D) plasma and magnetic field equilibrium. This new method allows for modeling larger plasma sheet domains and is less detrimental to numerical instability than other Euler-potential methods. In this study, we used this new method to establish the empirical pressure and magnetic field equilibria.

[7] Here we obtain the force-balanced magnetic field configurations under different levels of *Kp* and solar wind dynamic pressure (P_{SW}) using the observed equatorial isotropic plasma pressure distribution as an input to the 3-D equilibrium magnetic field model of *Zaharia* [2008]. Our pressure distribution is statistical (see Figure 1 of *Wang et al.* [2013]), so we chose *Kp* since its 3 h average is more likely to reflect equilibrium conditions under different levels of solar wind driving than other shorter time scale indices that reflect specific disturbances. We also chose P_{SW} since it has been shown to strongly regulate the plasma sheet pressure [*Borovsky et al.*, 1998]. Details of our modeling are described in section 2. In contrast to the simple pressure input used in *Zaharia et al.* [2004] which is based mainly on a quiet time empirical 1-D pressure profile along midnight, here we use realistic plasma pressure profiles from an empirical 2-D pressure model established in *Wang et al.* [2013] using Geotail and THEMIS observations. As discussed in *Wang et al.* [2013], with these more realistic plasma pressure profiles, we obtained magnetic field configurations in fairly good agreement with observations. The characteristics of the force-balanced magnetic field and how it changes with *Kp* and P_{SW} are described in section 3. The stability of the 3-D pressure and magnetic field configurations and the major differences between our magnetic field and the non-force-balanced Tsyganenko 89 (T89) magnetic field model [*Tsyganenko*, 1989] are discussed in section 4.

2. Modeling

[8] The magnetic field model of *Zaharia* [2008] obtains the magnetic field by solving the single-fluid force balance equation $\nabla P=\mathbf{J}\times\mathbf{B}$ in terms of Euler potentials as $\mathbf{B}=\nabla\alpha\times\nabla\beta$, where P is plasma pressure. In this model P can be either isotropic or anisotropic and, as described below, we assumed isotropic P in this study. The 3-D force balance equation can be decoupled into two coupled "quasi-2-D" equations in the directions parallel to $(\mathbf{B}\times\nabla\alpha)$ and $(\mathbf{B}\times\nabla\beta)$, respectively, as follows:

$$\mathbf{J}\cdot\nabla\alpha=\nabla\cdot\left[(\nabla\alpha)^2\nabla\beta-(\nabla\alpha\cdot\nabla\beta)\nabla\alpha\right]=-\frac{\partial P}{\partial\beta} \quad (1)$$

$$\mathbf{J}\cdot\nabla\beta=\nabla\cdot\left[(\nabla\beta\cdot\nabla\alpha)\nabla\beta-(\nabla\beta)^2\nabla\alpha\right]=-\frac{\partial P}{\partial\alpha} \quad (2)$$

in rationalized emu.

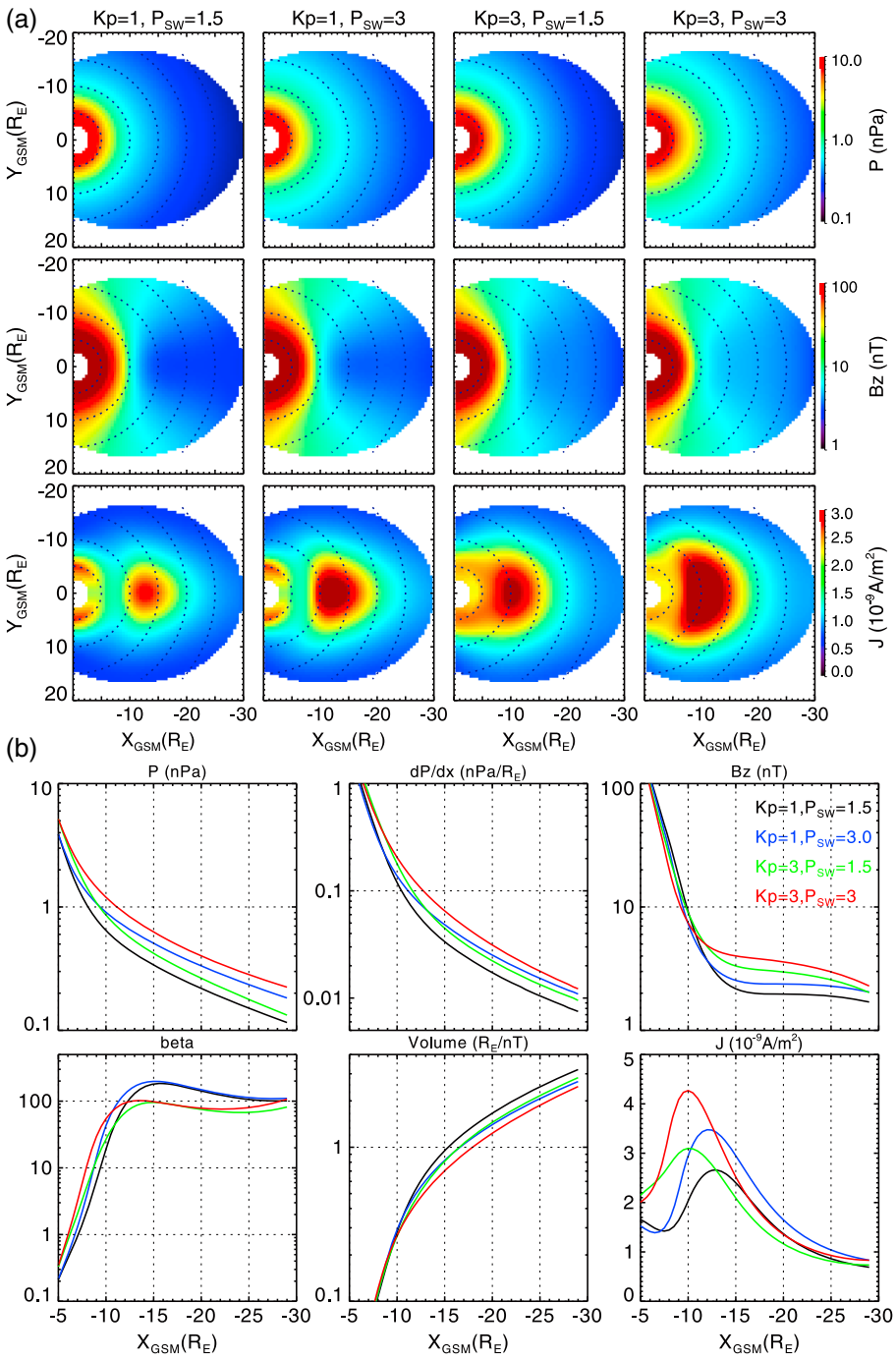

Figure 2. (a) Plasma pressure, *Bz* and westward J_ϕ on the nightside equatorial plane for the four cases. (b) The midnight radial profiles of equatorial plasma pressure, plasma pressure gradient, *Bz*, plasma beta, flux tube volume per unit flux from the equatorial plane to the ionosphere, and westward J_ϕ for the four cases (black: $Kp = 1$, $P_{SW} = 1.5$ nPa; blue: $Kp = 1$, $P_{SW} = 3.0$ nPa; green: $Kp = 3$, $P_{SW} = 1.5$ nPa; red: $Kp = 3$, $P_{SW} = 3.0$ nPa).

[9] The constant α and β surfaces are found from solving the equations 1 and 2 numerically, through an alternating iterative process. Both boundary conditions and the inhomogeneous terms on the right-hand sides $\left(\frac{\partial P}{\partial \alpha} \text{and} \frac{\partial P}{\partial \beta}\right)$ need to be prescribed.

[10] Here, the pair of Euler potentials (α, β) are chosen as below:

$$\alpha' = \alpha + F(\beta)$$
$$\beta' = \beta$$

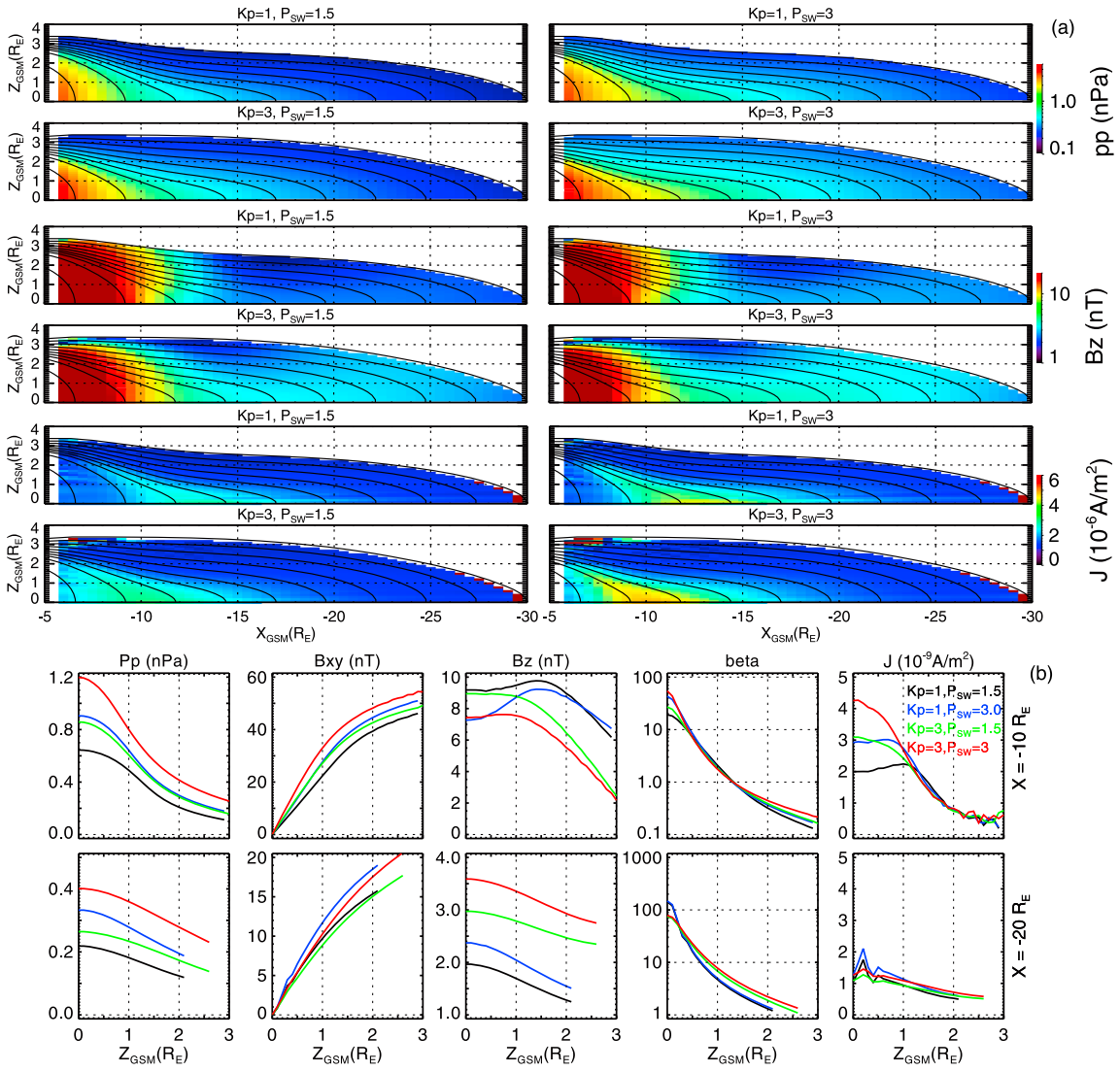

Figure 3. (a) Plasma pressure, *Bz*, and westward J_ϕ in the midnight *X*-*Z* plane for the four cases. The black curves are magnetic field lines. (b) The *Z* profiles of plasma pressure, *Bxy*, *Bz*, plasma beta, and westward J_ϕ at $Y=0$ and $X=-10$ and -20 R_E for the four cases (black: $Kp=1$, $P_{SW}=1.5$ nPa; blue: $Kp=1$, $P_{SW}=3.0$ nPa; green: $Kp=3$, $P_{SW}=1.5$ nPa; red: $Kp=3$, $P_{SW}=3.0$ nPa).

with $F(\beta)$ to be determined. Here α is defined to be proportional to the poloidal magnetic flux into the Earth, the other potential β is chosen to be equivalent to the azimuthal angle. Since β is equivalent to the azimuthal angle, $F(\beta)$ must be periodic, that is, $F(\beta+2\pi)=F(\beta)$. The outer boundary condition for a' is obtained by tracing empirical magnetic field from a prescribed ellipse shape (see Figure 2a, X_{GSM} is from 0 to -30 R_E and the maximum $|Y_{GSM}|$ is 16 R_E) on the equatorial plane. Since in this study we investigate the magnetic field configurations corresponding to different *Kp* levels, we use the Tsyganenko 89 magnetic field model (T89) to prescribe the boundary conditions. By obtaining $F(\beta)$ through prescribing an outer contour of α, the freedom of choosing the inner contour disappears; a more complete description of this model has been given by *Zaharia* [2008]. The third coordinate, χ, determines the position along the field line and completes the nonorthogonal flux coordinate system (α, β, χ).

[11] The two pressure gradients, $\frac{\partial P}{\partial \alpha}$ and $\frac{\partial P}{\partial \beta}$ in 1 and 2 are prescribed by a given pressure spatial profile. In order to prescribe realistic pressure profiles, in *Wang et al.* [2013] we established empirical equatorial pressure distributions using Geotail and THEMIS observations. Pressure is assumed to be constant along each field line, which is the case with isotropic pressure. In situ observations have shown that the plasma sheet is quite isotropic [e.g., *Stiles et al.*, 1978; *Baumjohann and Paschmann*, 1989; *Nakamura et al.*, 1991; *Kaufmann et al.*, 2001], and strong pressure anisotropy is seen only in the inner magnetosphere [e.g., *Lui and Hamilton*, 1992; *De Michelis et al.*, 1999; *Wang et al.*, 2011]. Therefore, we assume isotropic pressure throughout our model domain.

[12] The prescribed pressure is kept spatially fixed on the equatorial plane and $P(\alpha, \beta)$ changes at each iteration as α and β change. The iteration process is repeated until the $\alpha=$ cont. and $\beta=$ const. surfaces converge to some tolerance, that is, when the cumulative difference between

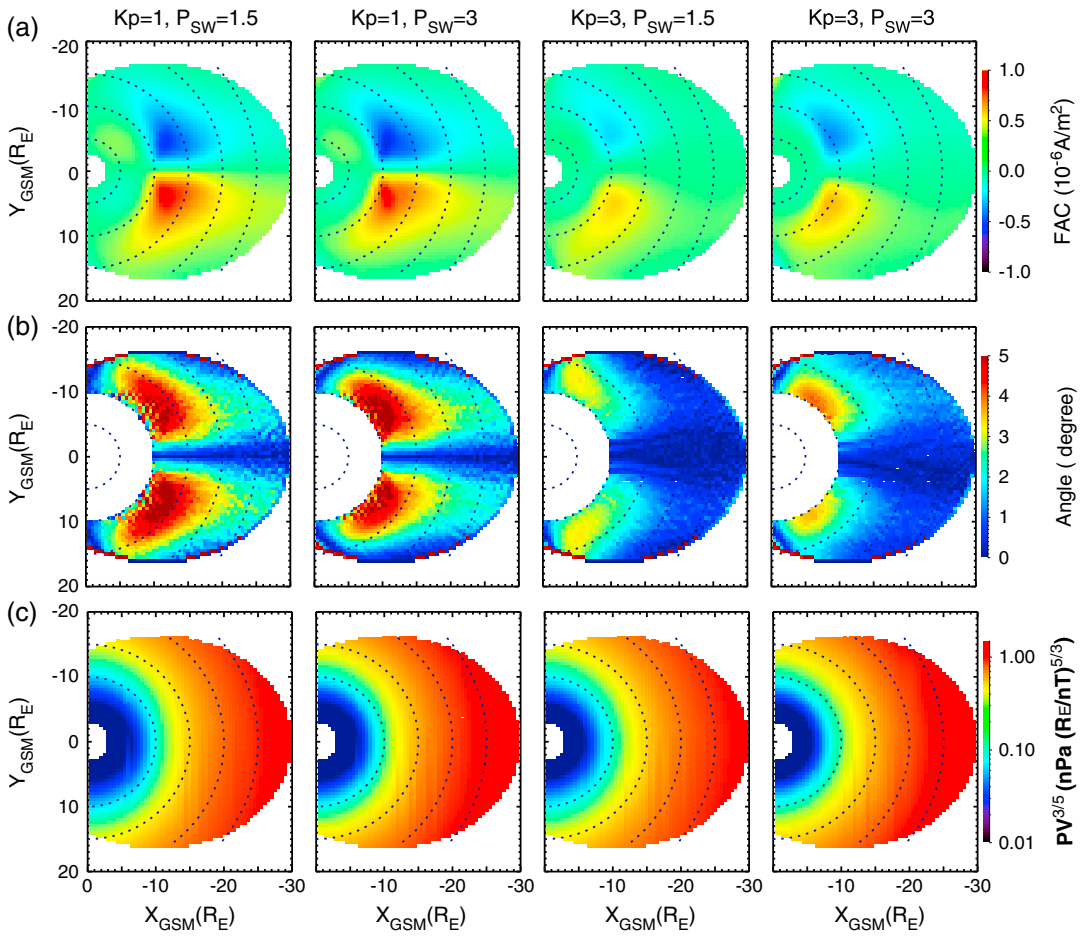

Figure 4. (a) The ionospheric FACs mapped to equatorial plane and (b) the magnitude of the angles between ∇V and ∇P_{eq} for the four cases. (c) $PV^{5/3}$ distributions on the equatorial plane.

α or β between two consecutive iterations decreases to a specified amount (here set to be 0.5%), indicating force balance is achieved.

[13] To understand the characteristic differences in the configurations in response to increasing *Kp* and P_{SW}, we computed force-balanced magnetic field for $Kp = 1$ and 3 and $P_{SW} = 1.5$ and 3 nPa using the observational pressure distribution model from *Wang et al.* [2013]. For the same *Kp* but different P_{SW} levels, the same magnetic field boundary conditions were used. Figure 1 shows that differences between ∇P and $\mathbf{J} \times \mathbf{B}$ for the four cases are only about 1%, indicating very good force balance.

3. Results

[14] By using the empirical pressure profiles as an input to our 3-D force-balanced model, equilibrium magnetic field configurations are obtained. In this section, we examine how the pressure, magnetic field and current density profile in the equatorial plane and along the midnight meridian change differently with increasing geomagnetic activity (*Kp*) and solar wind dynamic pressure (P_{SW}).

3.1. Equatorial Distributions and Midnight Radial Profiles

[15] Figure 2 shows the observational plasma pressure model, and the self-consistently modeled *Bz* and westward azimuthal current density (J_ϕ) in the equatorial plane, for the four cases. From Figure 2a, the plasma pressure has no significant azimuthal variation, and *Bz* is smaller at midnight than near the flanks while J_ϕ peaks around midnight. No dawn-dusk asymmetry is found. Along the midnight meridian as shown in Figure 2b, plasma pressure, pressure gradient, and *Bz* increase, while plasma beta and magnetic flux tube volume decrease, with decreasing radial distance (*r*). The pressure and pressure gradient increase as *Kp* or P_{SW} increases. Here flux tube volume has been taken from the equatorial plane to the ionosphere. However, the *Kp* effect dominates in the near-Earth region inside $r \sim 10\ R_E$ (comparing the black with green curves or the blue with red curves) while P_{SW} affects plasma pressure mainly in the tail (comparing the black with blue curves or the green with red curves). As *Kp* increases, stronger convection electric field (see Figure 1f of *Wang et al.* [2013], the median cross polar-cap potential is ~30 kV for $Kp = 1$ and ~70 kV for $Kp = 3$) pushes the plasma sheet further inward, resulting in a larger increase in pressure in the near-Earth region than in the tail. To maintain force balance with this increased pressure gradient force, *Bz* closer to the Earth decreases and increases in the tail while the J_ϕ peak intensifies and moves earthward and J_ϕ in the tail weakens. Accordingly, plasma beta increases in the inner magnetosphere and decreases in the tail. Additionally, the *Bz* changes cause the flux tube volume to decrease in

the tail but increase in the near-Earth. As discussed in section 3.4, magnetic field lines become more stretched.

[16] The effect of increasing P_{SW} is global compression of the magnetosphere. As shown in Figure 3 of *Wang et al.* [2013], the effect on the plasma pressure is more significant in the tail than in the near-Earth region. As a result, there are overall increases in Bz and J_ϕ in the tail (in contrast to the decreasing J_ϕ with increasing Kp) but much smaller changes in the near-Earth region compared with the Kp effect. The plasma beta in the tail, on the other hand, remains similar as P_{SW} increases.

3.2. Variations in the *Z* Direction

[17] The model results in the midnight meridian plane are shown in Figure 3a, and their variations with Z at $X=-10$ and -20 R_E are shown in Figure 3b. Plasma pressure decreases with increasing Z, since pressure is constant along field lines and field lines at higher Z map to larger equatorial distance where pressure is smaller. Bz, on the other hand, does not decrease monotonically with increasing r and Z. There is positive dBz/dr at $Z \geq \sim 1$ R_E beyond $X \sim -10$ R_E, and this feature moves earthward as Kp and P_{SW} increase. There is positive dBz/dz at $X \sim -10$ R_E in some cases. The positive dBz/dz has been observed by THEMIS [*Saito et al.*, 2010, 2011]; however, no corresponding local Bz minimum in the equator plane as predicted by Saito et al. is seen in our magnetic field.

[18] The B_{XY} increases with Z. At the same Z, B_{XY} increases with increasing P_{SW} regardless of radial distance, but at the higher Kp, B_{XY} increases at smaller r but decreases at larger r. As a result of the P decrease and B_{XY} increase, plasma beta decreases very quickly with increasing Z. Comparing the Z profiles of the B_{XY} with the Harris current sheet model [*Harris*, 1962] shows the current sheet thickness for $Kp=1$ decreases from ~ 3 R_E just within the outer boundary at $X=-30$ R_E to ~ 1.4 at $X=-13$ and then increases again slightly to ~ 1.8 R_E at $X=-10$ R_E. The thickness minimum is collocated with the equatorial J_ϕ peak. As the plasma sheet moves earthward under higher Kp, the minimum also moves to inside $X \sim -10$ R_E while the overall thickness in the tail increases. The thickness and its X profile do not change significantly with increasing P_{SW}. Constant J_ϕ contours are approximately aligned with the field lines. Therefore, in the region earthward of the equatorial J_ϕ peak, J_ϕ at the same X is seen to first increase inside $Z \sim 1$ R_E then decrease with increasing Z, resembling a bifurcated current structure.

3.3. Field-Aligned Currents

[19] Figure 4 shows the equatorial mapping of integrated field-aligned current (FACs) density $J_{||}$ in the one ionosphere computed using the Vasyliunas equation [*Vasyliunas*, 1970, 1984]:

$$\frac{J_{||}}{B_{\text{iono}}} = \frac{\mathbf{B}_{\text{eq}}}{B_{\text{eq}}^2} \cdot \left(\nabla V \times \nabla P_{\text{eq}}\right)$$

where the subscripts "iono" and "eq" are referred to the values in the ionosphere and equatorial plane, respectively. Also shown is the magnitude of the angle between ∇V and ∇P_{eq} for the four cases. Note that the FACs close to the Earth (inside $r \sim 6$ R_E) are not reliable due to larger uncertainty in the plasma pressure and its azimuthal gradient. In the tail, there are downward (upward) FACs at the pre-midnight (post-midnight) MLTs, which is the Region 2 (R2) FACs. There is no Region 1 FACs generated inside 30 R_E, indicating that the R1 FACs shown in the statistical *Iijima and Potemra* [1976a] are likely located along more distant tail (higher latitudes) and/or open field lines, not covered by our model domain. In addition, the R2 FACs move earthward together with the plasma sheet as Kp increases, but their magnitudes decrease mainly due to the decrease in radial flux tube volume gradient as well as the angle between ∇V and ∇P_{eq} as shown in Figure 4b. With increasing P_{SW}, despite a decrease in dV/dr, the overall FAC magnitudes are enhanced mainly due to an increase in pressure gradient and the angle between ∇V and ∇P_{eq} as demonstrated in Figure 4b. Additionally, despite little changes in their equatorial locations, as discussed in section 3.4, their corresponding ionosphere locations do move equatorward due to the more stretched field lines. In addition, as shown in Figure 4c the total entropy $PV^{5/3}$ increases with increasing distance away from the Earth. The overall $PV^{5/3}$ has no clear change with increasing Kp. However, it increases with increasing P_{SW}, suggesting that the changes in pressures and flux tube volume associated with the P_{SW} effect are not simply due to adiabatic compression.

[20] Some previous studies have suggested that substantial R1 FACs could be formed in the plasma sheet [e.g., *Wing and Newell*, 2000; *Zaharia and Cheng*, 2003] However, *Wing and Newell* [2000] did not use a force-balanced magnetic field, limiting the validity of their results. *Zaharia and Cheng* [2003] used an artificial pressure profile having an assumed azimuthal pressure maximum at midnight closer to Earth, and an azimuthal pressure minimum farther down the tail. Their profile thus gives R2 FACs closer to the Earth and R1 FACs further away. On the other hand, *Zaharia* [2008] established 3-D force-balanced magnetic field with a pressure profile having almost no azimuthal variations and obtained only R2 FACs in the plasma sheet.

[21] FACs are determined by the angles between the gradients of V and P. As described in *Wang et al.* [2013], our analytical pressure model captures the smooth variations in the large-scale pressure. It shows azimuthal pressure gradients becoming smaller with increasing radial distance, but no change in the direction of the gradients (shown in *Wang et al.* [2013]). Thus, the R2 FACs are seen to extend to our tail boundary. However, our prediction of the directions of FACs at large radial distances is not with absolute confidence, since the azimuthal variations of the observed pressure there are very small and the statistical uncertainty is large as shown in *Wang et al.* [2013].

[22] *Iijima and Potemra* [1976b] showed that the R2 FACs are larger with higher auroral electroject index. However, a higher auroral electroject can be associated with transient mesoscale disturbances in the plasma sheet such as bursty bulk flows (BBFs) The strong effect of BBFs on ionospheric currents has been seen in observations [*Lyons et al.*, 2013] and in simulations, such as the RCM-E [*Yang et al.*, 2011], where BBFs generate mesoscale FACs with magnitudes comparable to or larger than those of the large-scale FACs. The BBFs create R2 sense FACs earthward of the BBFs and R1 sense FACs along the BBFs. BBFs are more frequent during higher Kp, however, such transient mesoscale variations are averaged out in our long-term smooth pressure profiles so their associated mesoscale FACs are not added into our large-scale FACs.

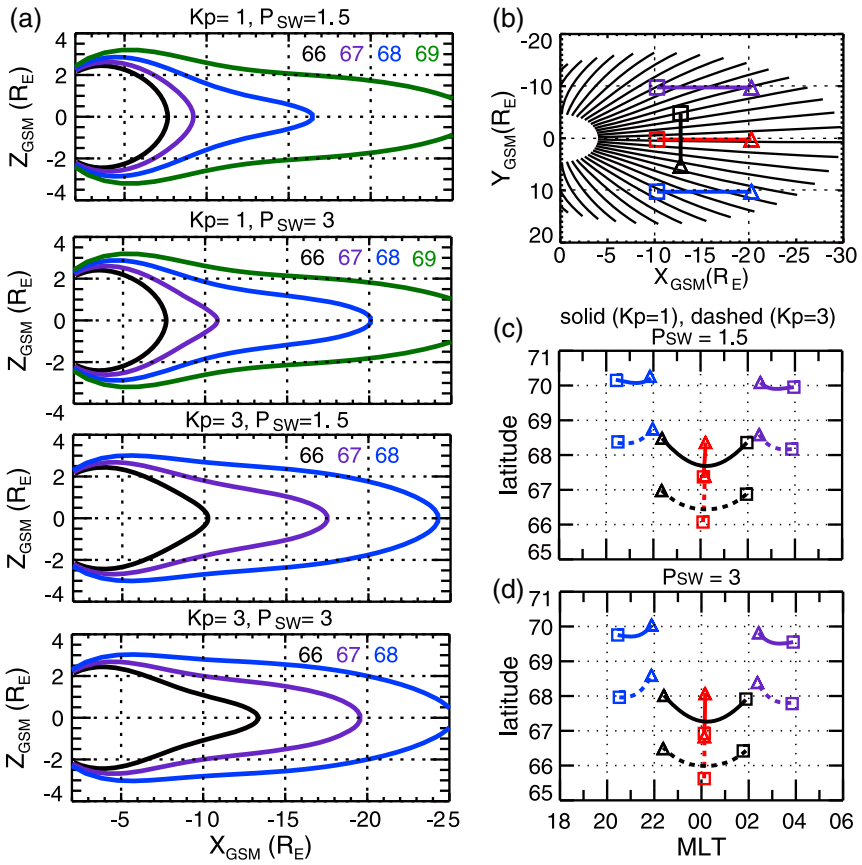

Figure 5. (a) Magnetic field lines from different ionospheric latitudes (66°: black curves; 67°: purple curves; 68°: blue curves; 69°: green curves) for the four cases. (c) Comparisons of the mapping latitudes between $Kp = 1$ (the solid curves) and $Kp = 3$ (the dashed curves) for different equator locations shown in Figure 5b under (top) $P_{SW} = 1$ and (bottom) $P_{SW} = 3$ nPa.

3.4. Field Line Mapping

[23] Magnetic field mapping is one of the most important applications of a given magnetic field configuration. Figure 5 shows comparisons of magnetic field line mappings for the different Kp and P_{SW}. Figure 5a shows the field lines originating from different ionosphere latitudes. As Kp or P_{SW} increases, the magnetic field lines become more stretched with more significant stretching corresponding to the increasing Kp. Figure 5c shows the ionosphere mapping of the four equatorial line-segment locations shown in Figure 5b. At the same X, the field lines at smaller $|Y|$ are mapped to lower ionospheric latitudes due to more stretched field lines at midnight than other MLTs. For structures along the same Y, the ionospheric mapping locations are aligned nearly longitudinally at midnight but become aligned much more latitudinally away from midnight. There is a slight dawn-dusk asymmetry with lower mapping latitudes at the post-midnight MLTs. The overall mapping latitudes are up to 0.5° lower as P_{SW} doubles but can be more than 1° lower as Kp changes from 1 to 3. It is important to remember that an observed equatorward (poleward) motion of ionospheric phenomena, for example aurora, does not necessarily correspond to an earthward (tailward) motion in the equatorial plane, and thus ionosphere motion may simply be associated with a change in the field line mapping.

4. Discussion

4.1. Stability

[24] Plasma instability in the Earth's magnetosphere has been discussed in many studies, including large-scale interchange in-

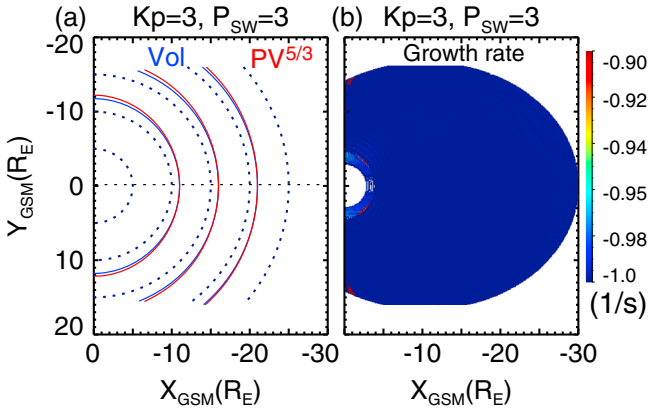

Figure 6. Illustration of interchange instability. (a) Contours of constant flux tube volume (Vol) and $PV^{5/3}$ in the equatorial plane and (b) the growth rate for interchange instability for $Kp = 3$ and $P_{SW} = 3$ nPa case.

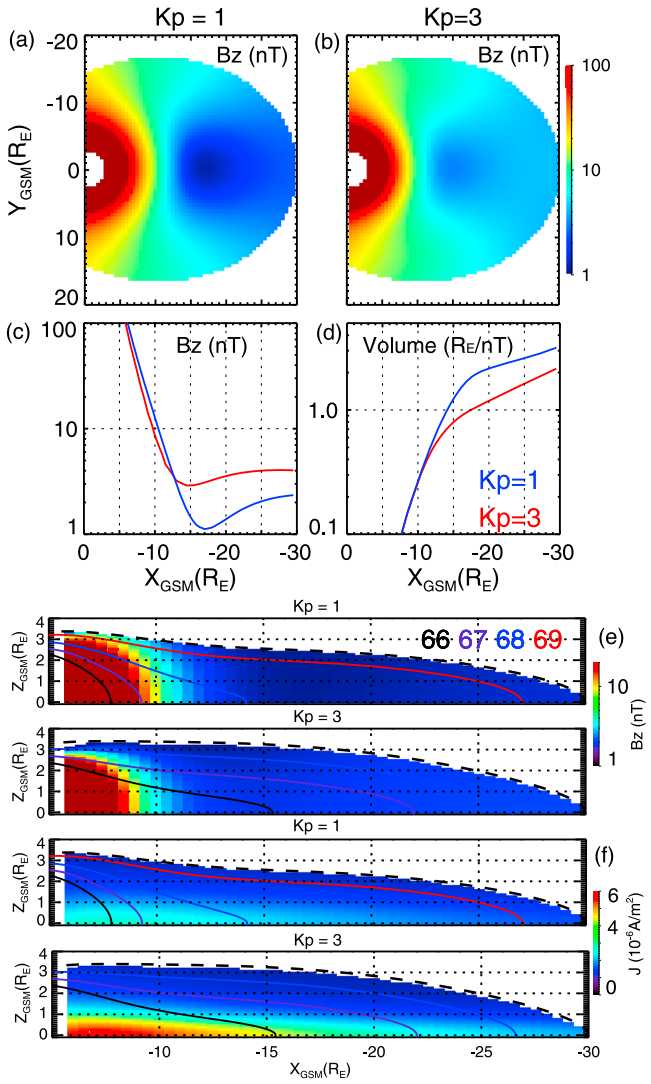

Figure 7. The T89 *Bz* in the equatorial plane for (a) $Kp = 1$ and (b) $Kp = 3$. The midnight radial profiles of (c) equatorial *Bz* and (d) flux tube volume form the T89 model for $Kp = 1$ (the blue curves) and $Kp = 3$ (the red curves). The *X*-*Z* profiles of (e) *Bz* and (f) westward J_ϕ along the midnight meridian from the T89 model for $Kp = 1$ and $Kp = 3$. The curves represent the T89 magnetic field lines from different ionosphere latitudes (66°: black, 67°: purple, 68°: blue, 69°: red).

stability [*Cheng*, 1985; *Southwood and Kivelson*, 1987; *Xing and Wolf*, 2007; *Xing*, 2008] and localized, explosive ballooning instability [*Cheng and Qian*, 1994; *Cheng and Lui*, 1998]. To examine whether our pressure and magnetic field equilibriums are susceptible to interchange instability, we computed the growth rate against long wavelength perturbation $r \propto -\cos\alpha + \frac{\beta R}{2\left(1+\frac{5}{6}\beta\right)}$ [*Xing*, 2008; (X. Xing and R. A. Wolf, Criterion for interchange instability in the Earth's plasma sheet, in preparation for *Journal of Geophysical Research*, 2013)] where α is the angle between $\nabla PV^{5/3}$ and ∇V, $R = \frac{V}{PV^{5/3}}\left|\frac{\delta\left(PV^{5/3}\right)}{\delta V}\right|$, and β is the plasma beta averaged over the entire flux tube. Figure 6a shows contour lines of flux tube volume and $PV^{5/3}$ for the $Kp = 3$ and $P_{SW} = 3$ nPa case. The two sets of lines are aligned with each other near midnight and have angles much smaller than $\pi/2$ in the flanks, implying that the plasma sheet is interchange stable [*Xing and Wolf*, 2007]. Figure 6b shows the growth rates estimated under the same conditions, the growth rates being close to -1 over the entire calculation domain of the plasma sheet. Similar values for growth rates are found for all other cases, indicating that the plasma sheet is interchange stable, consistent with the conclusion of *Xing and Wolf* [2007] where nonforce-balanced empirical plasma pressure and magnetic field models were used.

[25] As discussed in previous studies [e.g., *Lui et al.*, 1992; *Cheng and Lui*, 1998; *Cheng and Zaharia*, 2004], the criterion for the ballooning instability requires high plasma beta (>50), and the most unstable modes are located in the strong cross-tail current sheet region [*Cheng and Lui*, 1998; *Cheng and Zaharia*, 2004]. As shown in Figure 2, the high beta region (beta > 50) is confined in tail region ($X < -10\ R_E$) and around midnight ($|Y| < 10\ R_E$) (not shown here). The peak of cross-tail current is at *r* from 10 to 15 R_E, depending on activity level and solar wind driving, indicating that this is the most likely region to be unstable to the ballooning modes. This is also consistent with *Cheng and Zaharia* [2004]. However, future studies are needed to investigate the ballooning instability in detail.

4.2. Comparisons With the Non-Force-Balanced T89 Magnetic Field

[26] We compare our force-balanced magnetic field configurations with the statistical Geotail and THEMIS magnetic field profiles in *Wang et al.* [2013] and find fairly good agreement. In this section, we investigate if there are any characteristic differences between our magnetic field and the T89 field, which is not force balanced. The T89 is built by fitting the model field generated from a framework of postulated currents, including the ring current, tail current and magnetopause current as well as including the effect of warping the tail current sheet, to observed magnetic fields. Several studies have evaluated the T89 magnetic field against observations. *Weiss et al.* [1997] used a database of magnetic conjunctions between DMSP at low altitudes and LANL

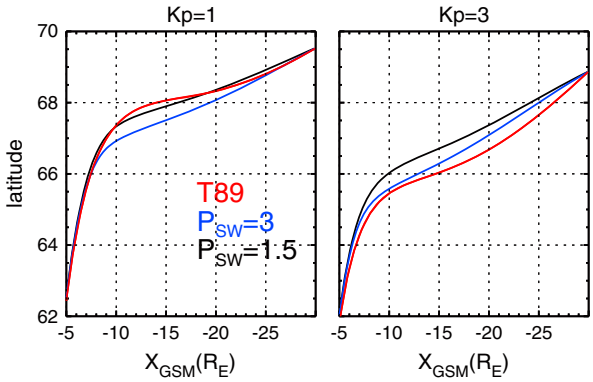

Figure 8. The mapping ionosphere latitudes versus the corresponding equatorial radial distance at midnight for (left) $Kp = 1$ and (right) $Kp = 3$ from the T89 and our model. The T89 results are shown in red and our results for $Kp = 1$ in black and $Kp = 3$ in blue.

satellites at geosynchronous orbit to evaluate the accuracy of T89. They found that T89 is understretched at geosynchronous orbit. In addition, *McCollough et al*. [2008] did a statistical comparison of commonly used external magnetic field models and concluded that T89 can only provide gross pictures of magnetosphere during quiet times, and does not predict well the dayside magnetic field.

[27] Figure 7 shows the T89 magnetic field and J_φ for $Kp = 1$ and $Kp = 3$. From Figures 7a, 7b, and 7d, the equatorial Bz profiles and the increase in the tail Bz and decrease in flux tube volume with increasing Kp are qualitatively consistent with our results. However, there are three major differences from our magnetic field. As shown in Figures 7c, the equatorial dBz/dr becomes positive beyond $X \sim -15\ R_E$ so that a local Bz minimum can be seen in the equatorial plane for both Kp levels. Also there is no positive dBz/dz anywhere in the T89 field as shown in Figure 7e. In addition, the T89 J_ϕ contours are not aligned with field lines so that currents always peak at the equator and monotonically decrease with increasing Z as shown in Figure 7f.

[28] Figure 8 shows the difference of magnetic field lines mapping between our field and the T89 for $Kp = 1$ and $Kp = 3$. For $Kp = 1$, T89 mapping latitudes are very similar to our results for $Kp = 1$ and $P_{SW} = 1.5$ nPa. This indicates that the T89 can well represent the quiet time magnetic field configuration, consistent with the evaluation of *McCollough et al*. [2008]. For $Kp = 3$, the T89 maps to lower latitudes (up to 1°) compared with our model, indicating the T89 is over stretched during higher Kp levels as compared to our model.

5. Summary

[29] A realistic magnetic field configuration is crucial to understanding plasma sheet dynamics and M-I coupling. In this study, by using empirical pressure profiles established from THEMIS and Geotail observations for different Kp and P_{SW} levels, the 3-D equilibrium magnetic field is obtained from the 3-D force balance magnetic field model. We have found the following:

[30] 1. The plasma sheet inner boundary moves earthward as Kp increases, resulting in a substantial pressure increase near the Earth, while magnetosphere compression during higher P_{SW} leads to pressure enhancement in the tail plasma sheet.

[31] 2. In response to the increased plasma pressure during higher Kp and P_{SW}, enhanced J_ϕ decreases (increases) the Bz in the region earthward (tailward) of the J_ϕ peak. Relative to the changes from increasing P_{SW}, the Kp associated pressure enhancement causes the J_ϕ peak to move further earthward and the field lines to become more stretched.

[32] 3. In comparison with the non-force-balanced T89 magnetic field, there is no equatorial Bz minimum found for the considered pressure profiles. There is positive dBz/dz in the near-Earth region in most of the cases. A similar positive dBz/dz has been observed by THEMIS. Bifurcation of J_ϕ appears in the near-Earth area as a result of our J_ϕ configuration being approximately aligned with field lines, while the T89 J_ϕ decreases monotonically with increasing Z everywhere.

[33] 4. Peaks of the R 2 FACs are near the inner edge of the plasma sheet, and the FACs increase (decrease) as P_{SW} (Kp) increases.

[34] 5. Field lines become more stretched and the mapping latitude of a fixed equatorial location is lower as Kp and P_{SW} increase, and more significant differences in the stretching and latitudes are associated with the Kp change. Mapping latitudes are slightly lower in the post-midnight than pre-midnight MLTs. In comparison, the T89 mapping latitudes are higher (lower) than our fields for $Kp = 1$ ($Kp = 3$).

[35] 6. The force-balanced pressure and magnetic field configurations for all Kp and P_{SW} are intrinsically stable to the interchange instability. However, the region near midnight may be unstable to the ballooning modes around $X = -15$ to $-10\ R_E$ due to very high beta and strong cross-tail current. An actual ballooning stability analysis, beyond the scope of this paper, would need to be performed to test this possibility.

[36] **Acknowledgments.** The work by C.-P. Wang, C. Yue, X. Xing, and L. R. Lyons at UCLA has been supported by NASA grants NNX11AJ12G, NNX09AQ41H, and NNX08A135G, and NSF grants ATM-0819864 and ATM-1003595, as well as the IGPPS program at Los Alamos through a LANL/UCLA collaborative grant. The work by S. G. Zaharia has been supported by NSF grants 1131873 and 1203460, NASA grant NNH10AP09I and by the IGPPS Program at Los Alamos National Laboratory.

[37] Masaki Fujimoto thanks the reviewers for their assistance in evaluating this paper.

References

Baumjohann, W., and G. Paschmann (1989), Determination of the polytropic index in the plasma sheet, *Geophys. Res. Lett.*, *16*, 295–298.

Borovsky, J. E., M. F. Thomsen, and R. C. Elphic (1998), The driving of the plasma sheet by the solar wind, *J. Geophys. Res.*, *103*, 17,617–17,640.

Cheng, A. F. (1985), Magnetospheric interchange instability, *J. Geophys. Res.*, *90*, 9900–9904.

Cheng, C. Z. (1995), Three-dimensional magnetospheric equilibrium with isotropic pressure, *Geophys. Res. Lett.*, *22*, 2401–2404.

Cheng, C. Z., and A. T. Y. Lui (1998), Kinetic ballooning instability for substorm onset and current disruption observed by AMPTE/CCE, *Geophys. Res. Lett.*, *25*, 4091–4094, doi:10.1029/1998GL900093.

Cheng, C. Z., and Q. Qian (1994), Theory of ballooning-mirror instabilities for anisotropic pressure plasmas in the magnetosphere, *J. Geophys. Res.*, *99*, 11,193–11,210, doi:10.1029/94JA00657.

Cheng, C. Z., and S. Zaharia (2004), MHD ballooning instability in the plasma sheet, *Geophys. Res. Lett.*, *31*, L06809, doi:10.1029/2003GL018823.

De Michelis, P., I. A. Daglis, and G. Consolini (1999), An average image of proton plasma pressure and of current systems in the equatorial plane derived from AMPTE/CCE-CHEM measurements, *J. Geophys. Res.*, *104*, 28,615–28,624.

Gkioulidou, M., C.-P. Wang, and L. R. Lyons (2011), Effect of self-consistent magnetic field on plasma sheet penetration to the inner magnetosphere: Rice convection model simulations combined with modified Dungey force-balanced magnetic field solver, *J. Geophys. Res.*, *116*, A12213, doi:10.1029/2011JA016810.

Harris, E. G. (1962), On a plasma sheath separating regions of oppositely directed magnetic field, *Nuovo Cimento*, *XXIII*, 115.

Hesse, M., and J. Birn (1993), Three-dimensional magnetotail equilibria by numerical relaxation techniques, *J. Geophys. Res.*, *98*, 3973–3982.

Hori, T., K. Maezawa, Y. Saito, and T. Mukai (2000), Average profile of ion flow and convection electric field in the near-Earth plasma sheet, *Geophys. Res. Lett.*, *27*, 1623–1626.

Iijima, T., and T. A. Potemra (1976a), Field-aligned currents in the dayside cusp observed by Triad, *J. Geophys. Res.*, *81*, 5971–5979, doi:10.1029/JA081i034p05971.

Iijima, T., and T. A. Potemra (1976b), The amplitude distribution of field-aligned currents at northern high latitudes observed by Triad, *J. Geophys. Res.*, *81*, 2165–2174.

Kaufmann, R. L., B. M. Ball, W. R. Paterson, and L. A. Frank (2001), Plasma sheet thickness and electric currents, *J. Geophys. Res.*, *106*, 6179–6193.

Kistler, L. M., W. Baumjohann, T. Nagai, and E. Möbius (1993), Superposed epoch analysis of pressure and magnetic field configuration changes in the plasma sheet, *J. Geophys. Res.*, *98*, 9249–9258.

Liu, S., M. W. Chen, M. Schulz, and L. R. Lyons (2006), Initial simulation results of storm-time ring current in a self-consistent magnetic field model, *J. Geophys. Res.*, *111*, A04225, doi:10.1029/2005JA011194.

Lui, A. T. Y., and D. C. Hamilton (1992), Radial profiles of quiet time magnetospheric parameters, *J. Geophys. Res.*, *97*, 19,325–19,332.

Lui, A. T. Y., R. E. Lopez, B. J. Anderson, K. Takahashi, L. J. Zanetti, R. W. McEntire, and R. Strangeway (1992), Current disruptions in the near-Earth neutral sheet region, *J. Geophys. Res.*, *97*(A2), 1461–1480.

Lyons, L. R., Y. Nishimura, E. Donovan, and V. Angelopoulos (2013), Distinction between auroral substorm onset and traditional ground magnetic onset signatures, *J. Geophys. Res. Atmos.*, *118*, 4080–4092, doi:10.1002/jgra.50384.

McCollough, J. P., J. L. Gannon, D. N. Baker, and M. Gehmeyr (2008), A statistical comparison of commonly used external magnetic field models, *Space Weather*, *6*, S10001, doi:10.1029/2008SW000391.

Nakamura, M., G. Paschmann, W. Baumjohann, and N. Sckopke (1991), Ion distributions and flows near the neutral sheet, *J. Geophys. Res.*, *96*, 5631–5649.

Olson, W. P., and K. A. Pfitzer (1974), Quantitative model of magnetospheric magnetic-field, *J. Geophys. Res.*, *79*, 3739–3748.

Saito, M. H., L.-N. Hau, C.-C. Hung, Y.-T. Lai, and Y.-C. Chou (2010), Spatial profile of magnetic field in the near-Earth plasma sheet prior to dipolarization by THEMIS: Feature of minimum B, *Geophys. Res. Lett.*, *37*, L08106, doi:10.1029/2010GL042813.

Saito, M. H., D. Fairfield, G. Le, L.-N. Hau, V. Angelopoulos, J. P. McFadden, U. Auster, J. W. Bonnell, and D. Larson (2011), Structure, force balance, and evolution of incompressible cross-tail current sheet thinning, *J. Geophys. Res.*, *116*, A10217, doi:10.1029/2011JA016654.

Sergeev, V. A., and M. V. Malkov (1988), Diagnostics of the magnetic configuration of the plasma layer from measurements of energetic electrons above the ionosphere, *Geomagn. Aeron.*, *28*, 549.

Sergeev, V. A., E. M. Sazhina, N. A. Tsyganenko, J. A. Lundblad, and F. Soraas (1983), Pitch-angle scattering of energetic protons in the magnetotail current sheet as the dominant source of their isotropic precipitation into the nightside ionosphere, *Planet. Space Sci.* (ISSN 0032–0633), *31*, 1147–1155, doi:10.1016/0032-0633(83)90103-4.

Southwood, D. J., and M. G. Kivelson (1987), Magnetospheric interchange instability, *J. Geophys. Res.*, *92*, 109–116.

Speiser, T. W. (1965), Particle trajectories in a model current sheet, based on the open model of the magnetosphere, with applications to auroral particles, *J. Geophys. Res.*, *70*, 1717–1728, doi:10.1029/JZ070i007p01717.

Spence, H. E., M. G. Kivelson, R. J. Walker, and D. J. McComas (1989), Magnetospheric plasma pressures in the midnight meridian: Observations from 2.5 to 35 R_E, *J. Geophys. Res.*, *94*, 5264–5272.

Stiles, G. S., J. E. W. Hones Jr., S. J. Bame, and J. R. Asbridge (1978), Plasmasheet pressure anisotropies, *J. Geophys. Res.*, *83*, 3166–3172.

Toffoletto, F. R., R. W. Spiro, R. A. Wolf, M. Hesse, and J. Birn (2001), Modeling inner magnetospheric electrodynamics, in *Space Weather*, Geophys. Monogr. Ser., vol. *125*, edited by P. Song, H. J. Singer, and G. L. Siscoe, AGU, Washington, D. C., pp. 265–272.

Tsyganenko, N. A. (1989), A magnetospheric magnetic field model with a warped tail current sheet, *Planet. Space Sci.*, *37*, 5–20.

Tsyganenko, N. A. (1990), Quantitative models of magnetospheric magnetic field: Methods and results, *Space. Sci. Rev.*, *54*, 75.

Tsyganenko, N. A. (1995), Modeling the Earth's magnetospheric magnetic field confined within a realistic magnetopause, *J. Geophys. Res.*, *100*, 5599–5612.

Tsyganenko, N. A. (1996), Effects of the solar wind conditions on the global magnetospheric configuration as deduced from data-based field models, in *Proceedings of the ICS-3 Conference on Substorms*, *Eur. Space Agency Spec. Publ. 389*, pp. 181–185, Eur. Space Agency, Noordwijk, Netherlands.

Tsyganenko, N. A. (2010), On the reconstruction of magnetospheric plasma pressure distributions from empirical geomagnetic field models, *J. Geophys. Res.*, *115*, A07211, doi:10.1029/2009JA015012.

Vasyliunas, V. M. (1970), Mathematical models of magnetospheric convection and its coupling to the ionosphere, in *Particles and Fields in the Magnetosphere*, edited by B. M. McCormac, pp. 60–71, D. Reidel, Hingham, Mass.

Vasyliunas, V. M. (1984), Fundamentals of current description, *Magnetospheric Currents*, Geophys. Monogr. Ser., 28, edited by T. A. Potemra, pp. 63–66, AGU, Washington, D. C.

Wang, C.-P., L. R. Lyons, M. W. Chen, and R. A. Wolf (2002), Two-dimensional quiet time equilibrium for the inner plasma sheet protons and magnetic field, *Geophys. Res. Lett.*, *29*(24), 2186, doi:10.1029/2001GL013984.

Wang, C.-P., L. R. Lyons, M. W. Chen, and F. R. Toffoletto (2004), Modeling the transition of the inner plasma sheet from weak to enhanced convection, *J. Geophys. Res.*, *109*, A12202, doi:10.1029/2004JA010591.

Wang, C.-P., M. Gkioulidou, L. R. Lyons, R. A. Wolf, V. Angelopoulos, T. Nagai, J. M. Weygand, and A. T. Y. Lui (2011), Spatial distributions of ions and electrons from the plasma sheet to the inner magnetosphere: Comparisons between THEMIS-Geotail statistical results and the Rice convection model, *J. Geophys. Res.*, *116*, A11216, doi:10.1029/2011JA016809.

Wang, C.-P., C. Yue, S. Zaharia, X. Xing, L. Lyons, V. Angelopoulos, T. Nagai, and T. Lui (2013), Empirical modeling of plasma sheet pressure and three-dimensional force-balanced magnetospheric magnetic field structure: 1. Observation, *J. Geophys. Res. Space Physics*, *118*, doi:10.1002/jgra.50585.

Weiss, L. A., M. F. Thomsen, G. D. Reeves, and D. J. McComas (1997), An examination of the Tsyganenko (T89a) field model using a database of two-satellite magnetic conjunctions, *J. Geophys. Res.*, *102*, 4911–4918.

Wing, S., and P. T. Newell (1998), Central plasma sheet ion properties as inferred from ionospheric observation, *J. Geophys. Res.*, *103*, 6785–6800, doi:10.1029/97JA02994.

Wing, S., and P. T. Newell (2000), Quiet time plasma sheet ion pressure contribution to Birkeland currents, *J. Geophys. Res.*, *105*, 7793–7802, doi:10.1029/1999JA900464.

Wolf, R. A. (1983), The quasi-static (slow-flow) region of the magnetosphere, in *Solar-Terrestrial Physics*, pp. 303–368, Springer, The Netherlands.

Xing, X. (2008), *Criterion for interchange instability in the plasma sheet*, Rice University, Houston, Texas.

Xing, X., and R. A. Wolf (2007), Criterion for interchange instability in a plasma connected to a conducting ionosphere, *J. Geophys. Res.*, *112*, A12209, doi:10.1029/2007JA012535.

Yang, J., F. R. Toffoletto, R. A. Wolf, and S. Sazykin (2011), RCM-E simulation of ion acceleration during an idealized plasma sheet bubble injection, *J. Geophys. Res.*, *116*, A05207, doi:10.1029/2010JA016346.

Zaharia, S. (2008), Improved Euler potential method for three-dimensional magnetospheric equilibrium, *J. Geophys. Res.*, *113*, A08221, doi:10.1029/2008JA013325.

Zaharia, S., and C. Z. Cheng (2003), Can an isotropic plasma pressure distribution be in force balance with the T96 model field? *J. Geophys. Res.*, *108*(A11), 1412, doi:10.1029/2002JA009501.

Zaharia, S., C. Z. Cheng, and K. Maezawa (2004), 3-D force-balanced magnetospheric configurations, *Ann. Geophys.*, *22*, 251–265.